ACS Biomaterials SCIENCE & ENGINEERING
Cite This: ACS Biomater. Sci. Eng. XXXX, XXX, XXX−XXX
Article
pubs.acs.org/journal/abseba

Effects of Geometry on the Mechanics and Alignment of Three-Dimensional Engineered Microtissues

Prasenjit Bose,[†] Jeroen Eyckmans,[‡,§] Thao D. Nguyen,[∥] Christopher S. Chen,[‡,§] and Daniel H. Reich*[,†]

[†]Department of Physics and Astronomy, Johns Hopkins University, Baltimore, Maryland 21218, United States
[‡]Department of Biomedical Engineering and the Biological Design Center, Boston University, Boston, Massachusetts 02215, United States
[§]The Wyss Institute for Biologically Inspired Engineering, Harvard University, Boston, Massachusetts 02115, United States
[∥]Department of Mechanical Engineering, Johns Hopkins University, Baltimore, Maryland 21218, United States

Supporting Information

ABSTRACT: The structure and stiffness of the extracellular matrix (ECM) in living tissues play a significant role in facilitating cellular functions and maintaining tissue homeostasis. However, the wide variation and complexity in tissue composition across different tissue types make comparative study of the impact of matrix architecture and alignment on tissue mechanics difficult. Here we present a microtissue-based system capable of controlling the degree of ECM alignment in 3D self-assembled fibroblast-populated collagen matrix, anchored around multiple elastic micropillars. The pillars provide structural constraints, control matrix alignment, enable measurement of the microtissues' contractile forces, and provide the ability to apply tensile strain using magnetic particles. Utilizing finite element models (FEMs) to parametrize results of mechanical measurements, spatial variations in the microtissues' Young's moduli across different regions were shown to be correlated with the degree of ECM fiber alignment. The aligned regions were up to six times stiffer than the unaligned regions. The results were not affected by suppression of cellular contractile forces in matured microtissues. However, comparison to a distributed fiber anisotropic model shows that variations in fiber alignment alone cannot account for the variations in the observed moduli, indicating that fiber density and tissue geometry also play important roles in the microtissues' properties. These results suggest a complex interplay between mechanical boundary constraints, ECM alignment, density, and mechanics and offer an approach combining engineered microtissues and computational modeling to elucidate these relationships.

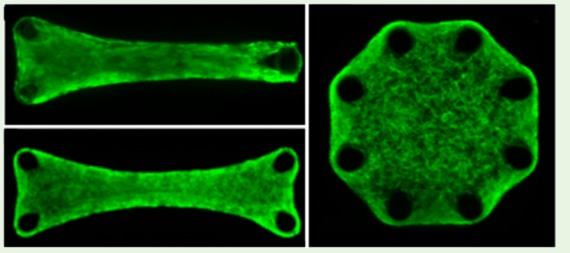

KEYWORDS: *engineered microtissues, extracellular matrix, alignment, density, mechanics, magnetic actuation*

1. INTRODUCTION

Cells in multicellular organisms reside in complex extracellular matrix (ECM) environments. The ECM is mostly composed of a three-dimensional (3D) network of fibrillar proteins, such as collagens and fibronectin. The composition and organization of these fibrillar networks vary substantially from one tissue type to another and results in tissues that have distinct mechanical properties. Numerous studies have shown that tissues consisting of highly aligned type I collagen such as tendon exhibit high stiffness,[1−4] whereas tissues consisting of more isotropic fiber orientations such as liver,[5] kidney,[6] or arterial wall[7,8] are relatively more compliant.[9] However, a major caveat to such studies is that in addition to ECM alignment, these tissues are comprised of vastly different cell types, cell densities, matrix compositions, fiber orientation, and matrix densities. In addition, cells respond in numerous ways to matrix architecture, and the ability to control ECM structure is critical for tissue engineering and efforts to advance understanding of mechanobiology at the cellular scale.[10] One approach to these challenges is to generate gels by direct polymerization from purified ECM components, such as type I collagen, and techniques have been developed to align the fibers before polymerization, such as through high magnetic fields,[11,12] extrusion,[13] electrospinning,[14] or shear-induced alignment.[15,16] It is important to note, however, that such polymerized gels generally have much lower density and stiffness compared to native tissues and are structurally very different from the ECMs assembled by living cells.

To bridge this gap between the complexity and lack of control over in vivo tissues, and the nonphysiologic nature of purified gels, approaches have been developed to embed cells within an ECM gel and then allow the cells to compact and

Special Issue: Biomaterials for Mechanobiology

Received: September 29, 2018
Accepted: December 6, 2018
Published: December 7, 2018

DOI: 10.1021/acsbiomaterials.8b01183
ACS Biomater. Sci. Eng. XXXX, XXX, XXX−XXX

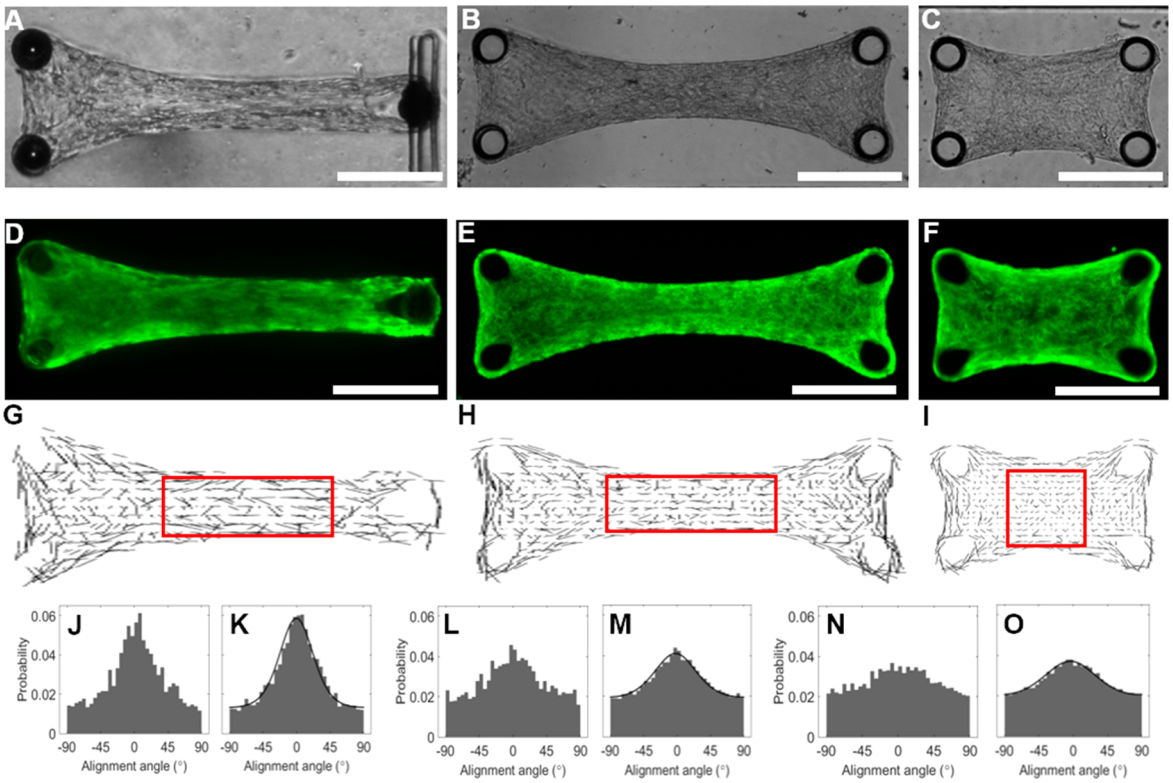

Figure 1. Anisotropic microtissues made from human dermal fibroblasts (HDFs) supported by (A) three pillars with tissue length to width ratio of 4:1 (triangular tissue), (B) four pillars with pillar spacing aspect ratio of 4:1, and (C) four pillars with pillar spacing aspect ratio of 2:1. (D−F) Corresponding epifluorescence images showing the fibronectin ECM networks in the tissues (scale bars = 300 μm). (G−I) ECM alignment maps of the tissues. (J, L, and N) Alignment angular distributions of central regions (red rectangles) of the triangular (J), 4:1 rectangular (L), and 2:1 rectangular (N) tissues. (K, M, and O) Average alignment angular distributions (N = 6) for the triangular (K), 4:1 rectangular (M), and 2:1 rectangular (O) tissues. The average distributions had widths 2σ of (K) 44° ± 2°, (M) 57° ± 3°, and (O) 75° ± 6°.

remodel the material to form tissue-like models.[17−22] Cellular contraction together with anisotropic external boundary constraints can be utilized to reorganize the initial isotropic matrix and can lead to alignment of fibers along the principal stress axis in these model tissues.[20,23] The aforementioned approach has been recently miniaturized, using poly(dimethylsiloxane) (PDMS) devices containing arrays of microwells fabricated with two vertical PDMS pillars protruding within them. Cell-laden collagen I mixtures seeded within the wells contracted around the pairs of pillars to form arrays of self-assembled, aligned 3D microtissues.[24−30] This system enables creation of microtissues with size scales of a few hundred micrometers, capable of both recapitulating macroscopic morphologies as well as generating tunable ECM fibrillar architectures utilizing only a few hundred cells.

In this study, we have expanded this microtissue gauge (μTUG) platform through the addition of multiple pillars and varied the geometry of the wells as a means to study how tissue alignment impacts its mechanics. The use of multipillared geometries allowed us to create microtissues with large regions of either unaligned or aligned ECM. This was achieved by controlling the pillar positions and their spacings; microtissues in wells with isotropically arranged pillars had a higher percentage of unaligned matrix, while anisotropic pillar positions led to development of tissues with a higher degree of aligned ECM. We used this new miniaturized platform to quantify the extent of ECM alignment in anisotropic vs isotropic microtissues, with both types of structures formed from cell-mediated ECM compaction under similar maturation conditions. Further, the pillars were designed to deflect in response to tissue-level forces, allowing measurement of forces at each pillar. Using magnetic beads attached to the tips of one pillar within each microtissue, quasi-static tensile loading of the microtissues provided a measure of their mechanical properties. Our results revealed that microtissues regions with aligned matrix are significantly stiffer than microtissues with regions of unaligned matrix and that the stiffness is not dependent on the degree of cellular contractility, for either aligned or isotropic ECM. As a means to assess the effects of geometry on stiffness in these engineered structures, we parametrized the low-strain properties of the microtissues via linear finite element models, and compared the range of effective Young's moduli of regions with different ECM alignment to the predictions of a distributed fiber anisotropic model developed previously to study native and engineered collagen tissues[31,32] to determine how matrix alignment affected tissue stiffnesses. Our analysis shows that both ECM fiber alignment and variations in fiber density arising from the cell-mediated compaction process influence the stiffness variations. As both of these factors can be controlled by the device geometry, these results suggest approaches to optimize such microtissues' structural and mechanical properties for desired applications.

2. MATERIALS AND METHODS

2.1. μTUG Device Fabrication. Arrays of multipillar μTUG devices were produced by replica molding. Initial, "master" versions of the devices were made from SU-8 photoresist (Microchem) on Si wafers, using a four-layered photolithography process as described

DOI: 10.1021/acsbiomaterials.8b01183
ACS Biomater. Sci. Eng. XXXX, XXX, XXX−XXX

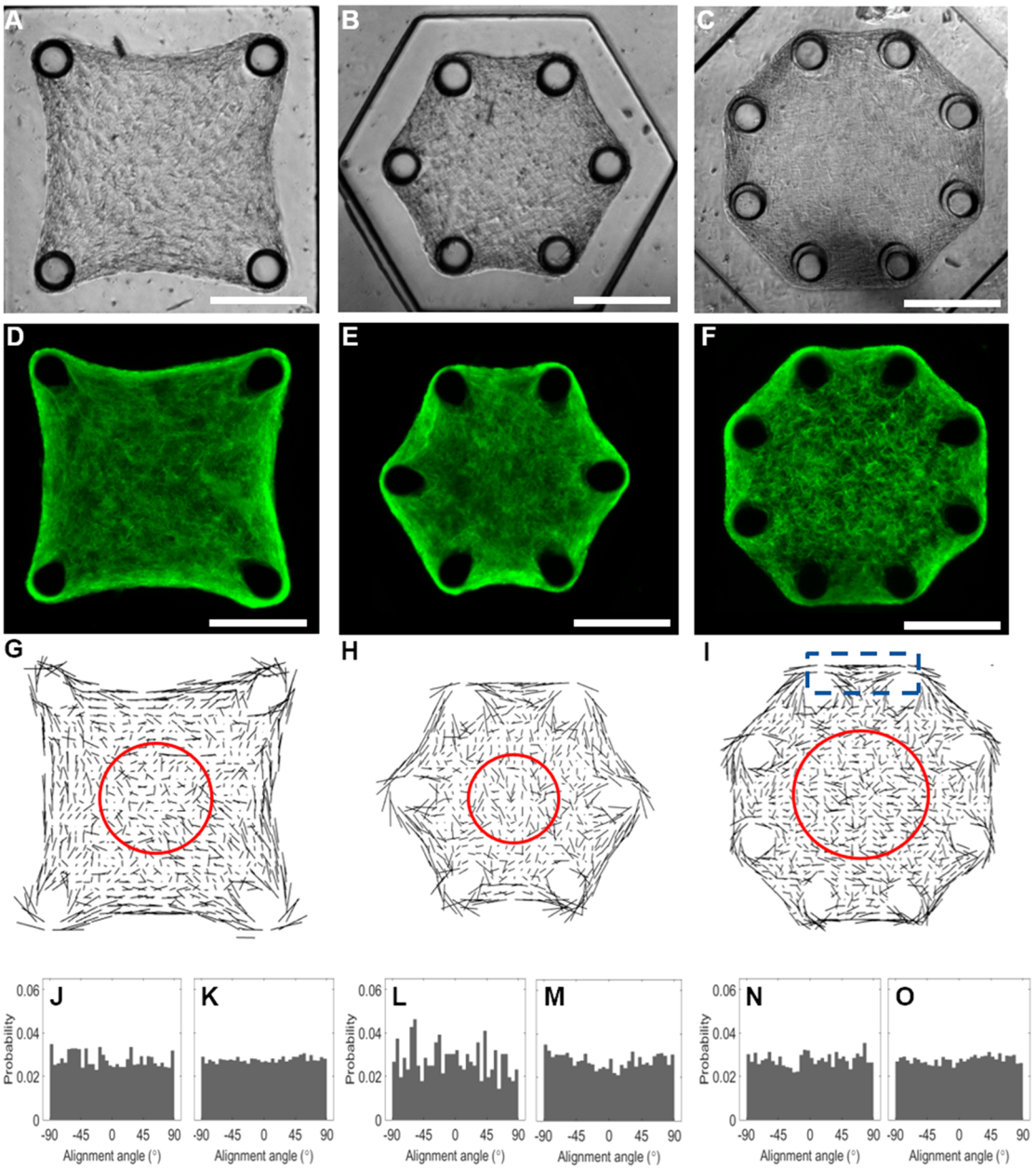

Figure 2. HDF microtissues with isotropic geometries: (A) square, (B) hexagonal, and (C) octagonal. (D−F) Corresponding epifluorescence images showing the fibronectin ECM networks in the tissues (scale bars = 300 μm). (G−I) ECM alignment maps of the tissues. (J, L, and N) Alignment angular distributions of central regions (red circles) of the square (J), hexagonal (L), octagonal (N) tissues. (K, M, and O) Average alignment angular distributions (N = 6) for the square (K), hexagonal (M), and octagonal (O) tissues. All of the isotropic tissues have local tangential ECM alignment around their edges as seen in the rectangular box in part I.

previously.[24,33,34] Poly(dimethylsiloxane) (PDMS) negative molds were made from the masters and the final μTUG devices were cast in PDMS from the molds. Six different μTUG well geometries with varying shapes, sizes, and pillar positions were used to control the microtissues' shape (Figures 1A−C and 2A−C). The pillars had circular cross sections to enable isotropic bending in two dimensions, with effective bending constant k = 1 μN/μm, except for the pillars at the apexes of the triangular μTUGs, which were rectangular in cross section to facilitate the application of unidirectional stretching forces, and which had k = 1.9 μN/μm in the loading direction. Details of the array dimensions, μTUG well geometries, and pillar dimensions are given in Supplementary Table S1. For magnetically actuated tensile loading experiments, approximately spherical Ni particles (Alfa Aesar no. 44739) with sizes varying from 76 to 116 μm were glued with PDMS on top of one pillar in each μTUG well.[27−29,34] $BaTiO_3$ spheres (Cospheric no. BTGMS-HI-4.15) of diameter 70−90 μm and refractive index n > 1.93 were attached with PDMS to the remaining pillars to enable tracking of their motion (Figure 3). The arrays were coated with 0.2% w/v Pluronic F-127 (Sigma-Aldrich no. P24443) prior to microtissue seeding to prevent adhesion of cells to the walls of the μTUG wells.[34]

2.2. Cell Culture and Microtissue Seeding. Human dermal fibroblasts (HDFs) (Gift from Maria Trojanowska, Boston University) and NIH 3T3 fibroblasts (ATCC) were cultured in 4.5 g/L Dulbecco's Modified Eagle Medium (DMEM) containing 10% fetal bovine serum (FBS), 100 units/mL penicillin, and 0.1 mg/mL streptomycin. The cells were maintained at 37 °C and 5% CO_2 and were passaged at a 1:5 ratio upon reaching confluence. For the experiments, cells at passage 8−14 (HDF) and <17 (3T3s) were suspended in 2 mg/mL rat-tail collagen type I (BD Bioscience) at a cell density of 1 × 10^5 cells/mL

DOI: 10.1021/acsbiomaterials.8b01183
ACS Biomater. Sci. Eng. XXXX, XXX, XXX−XXX

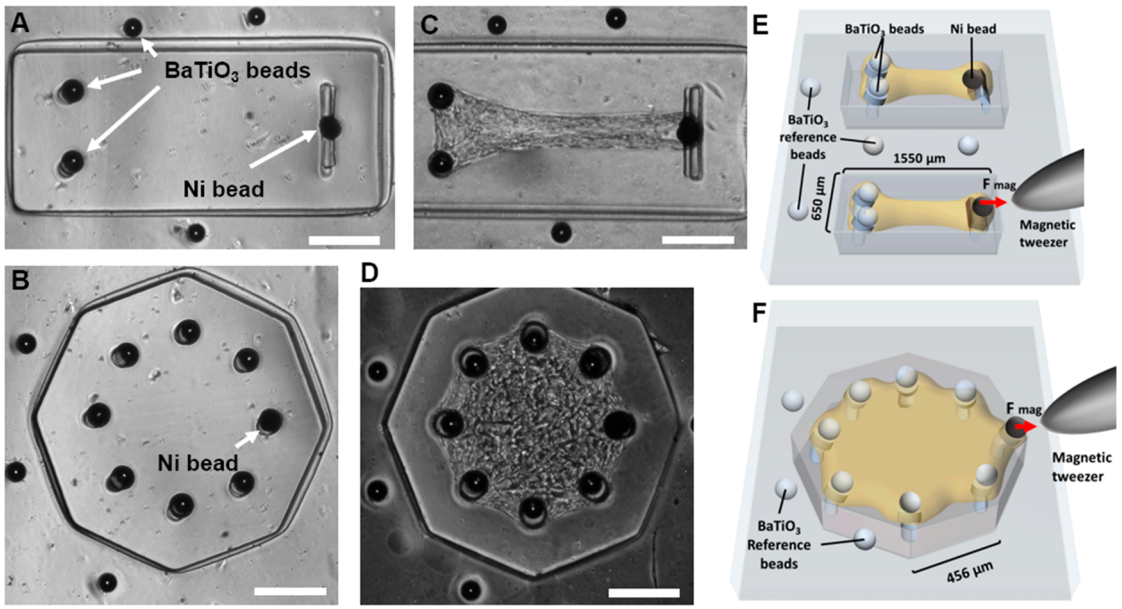

Figure 3. (A) Three-pillar μTUG well and (B) eight-pillar μTUG well showing $BaTiO_3$ on top of the pillars for displacement tracking and Ni beads on one pillar per well for magnetic actuation. Reference $BaTiO_3$ beads on the substrate enabled image registration. (C) Triangular and (D) octagonal microtissues on these structures after 72 h (scale bars = 300 μm). (E and F) Schematics of tissue stretching via force $\mathbf{F}_{mag}$ applied to magnetic beads via magnetic tweezers.

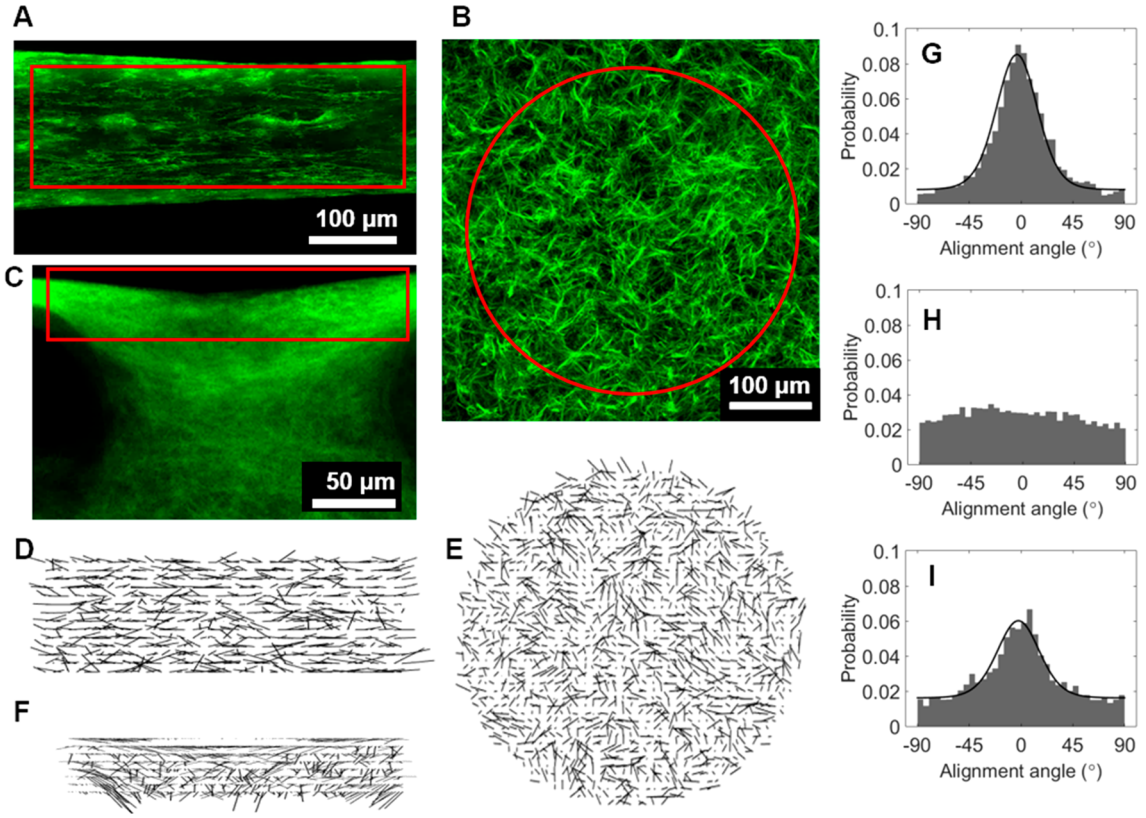

Figure 4. Confocal projections of the central region of (A) a triangular tissue and (B) an octagonal tissue and (C) right edge of the octagon (rectangular region shown in Figure 2I.) (D–F) Corresponding alignment maps of the fibronectin networks in panels A–C. (G–I) Angular alignment distributions for the maps in panels D–F. Widths 2σ: (G) 35° ± 1°, (I) 36° ± 3.

(150–200 cells per microtissue) for HDFs and 5×10^5 cells/mL (750–1000 cells per microtissue) for 3T3s and seeded into the microwells following previously published protocols.[24,26–28,30,34] The microtissues were allowed to self-assemble and compact in DMEM + 2% FBS (HDFs) or DMEM + 10% FBS (3T3s) for 72 h prior to the experiments. For the HDFs, it was necessary to use lower cell and FBS concentrations than for the 3T3s to compensate for the HDF's higher contractility and obtain stable microtissues.

2.3. Imaging. Phase contrast and epi-fluorescence images of the microtissues were taken using an inverted microscope (Nikon TE-

DOI: 10.1021/acsbiomaterials.8b01183
ACS Biomater. Sci. Eng. XXXX, XXX, XXX–XXX

2000) with a 4× air objective (Nikon Plan Fluor, NA = 0.13) and a CoolSnap HQ camera (Photometrics). For fluorescence images, the microtissues were fixed with 4% paraformaldehyde 72 h after seeding, washed in phosphate buffered saline (PBS), blocked in goat serum for 1 h at room temperature and incubated with primary antibodies for fibronectin (Abcam, cat no. ab194395) and rat-tail collagen type-I (Millipore, cat no. AB755P), both at 1:100 dilutions at 4 C. After overnight incubation, the microtissues were washed in PBS and incubated in secondary antibodies (Alexa-488 conjugated goat antimouse, Abcam, cat no. A-21121, and Alexa-568 conjugated goat antirabbit, Abcam, cat no. A-11011) and Hoechst (Life Technologies, cat no. H3570), all at 1:1000 dilution for 1 h at room temperature. For F-actin imaging, microtissues were treated with 0.1% Triton for 30 min post paraformaldehyde fixing, blocked in goat serum for 1 h at room temperature, and incubated in phalloidin (Alexa 568, Abcam, cat no. A-12380) at 1:500 dilution for 1 h at room temperature. Confocal images of the fluorescently labeled microtissues were collected using a Zeiss LSM 510 microscope and a 20× air objective (Zeiss Plan-Apochromat, NA = 0.8). Z-stack projections of the confocal images were obtained by averaging the image stacks in ImageJ.[35]

2.4. Matrix Alignment Quantification. Matrix alignment of the microtissues was measured using a custom Matlab (Mathworks) script based on the Fibriltool algorithm[36] applied to the fibronectin epifluorescence and confocal images of the microtissues. We calculated the normalized vector perpendicular to the local intensity gradient at each image pixel, $\mathbf{t} = (t_x, t_y) = \left(\frac{\partial I}{\partial y}, -\frac{\partial I}{\partial x}\right) / \sqrt{\left(\frac{\partial I}{\partial x}\right)^2 + \left(\frac{\partial I}{\partial y}\right)^2}$, utilizing near-neighbor finite differences and computed the local nematic tensor: $\mathbf{n} = \mathbf{t} \otimes \mathbf{t}$, where $n_{x,x} = t_x^2$, $n_{x,y} = n_{y,x} = t_x t_y$, and $n_{yy} = t_y^2$. To reduce effects due to pixilation in the images that led to small spurious alignment signals at ±45°, a Gaussian blur with standard deviation 1.5 pixels using the Matlab *Imgaussfilt* function was applied to the images prior to the gradient computation. To reduce noise, each image was subdivided into a grid of 5 pixel × 5 pixel squares, (5.4 μm × 5.4 μm for Figures 1, 2, S5, and S6 and 4.4 μm × 4.4 μm for Figure 4), and the average nematic (structure) tensor $\langle \mathbf{n} \rangle$ was computed for each grid square. The eigenvector $\mathbf{v}_1$ corresponding to the largest eigenvalue λ_1 of $\langle \mathbf{n} \rangle$ gave the average alignment direction in each grid square, and the difference in the two eigenvalues $q = \lambda_1 - \lambda_2$ gave a measure of the degree of alignment. Headless vector maps of $\mathbf{v}_1$ with lengths proportional to q were used to show the matrix alignment over the microtissue or a subregion of interest. In these maps the density of data points shown was reduced by a factor of 4 from the computed density for clarity. Histograms over subsections of the images were used to obtain alignment angular distributions.

2.5. Microtissue Stretching. Forces were applied successively to the "magnetic" pillar of each microtissue via a micromanipulator-controlled magnetic tweezer.[34,37] The magnetic field applied by the tweezer magnetized the pillar's Ni sphere and generated a force on the sphere, $\mathbf{F}_{mag} = \nabla(\boldsymbol{\mu}(\mathbf{B}) \bullet \mathbf{B})$, where $\boldsymbol{\mu}(\mathbf{B})$ is the sphere's magnetic moment. This force bent the magnetic pillar and caused the microtissue to stretch (Figure 3). Stretching experiments were conducted at 37 °C on an inverted microscope (Nikon TE-2000) equipped with a microscope enclosure incubator (InVivo Scientific) and a stage-mounted heating plate (TC-500, 20/20 Technology). Linearly ramped loading forces were applied to each microtissue over 120 s, producing microtissue strain rates of 0.005−0.05% per second. Phase contrast movies were recorded during stretching with a 4× objective at 20 frames/sec with a Prosilica GX-1050 camera (Allied Vision Technologies).

2.6. Force and Displacement Measurements. Stretching the microtissues caused displacements of the nonmagnetic pillars, which were measured by tracking the position of the $BaTiO_3$ beads attached to the pillar heads. The $BaTiO_3$ beads' high refractive index, $n > 1.93$, enabled them to function as spherical lenses in the media solution (Figure S1), and they produced sharp bright spots with full-width half-maximum (fwhm) 6.5 μm when imaged via phase contrast microscopy. The strong contrast between these spots and the dark regions around them (Figure 3) enabled high resolution tracking of the spots' centroids, and hence the pillar displacement vectors, to ±0.028 μm (±0.02 pixels) via standard particle tracking software.[38] The pillar displacements were converted to forces by multiplying by the pillars' bending constant, $k = 1$ μN/μm.[24,28,30] A texture correlation algorithm[39] applied to every 20th frame of the stretching movies over the whole microtissue body, excluding the pillars, yielded a mapping of the microtissues' displacement field over a initially rectangular grid. The initial grid spacing was 20 μm × 14 μm for triangular microtissues and 20 μm × 20 μm for octagonal microtissues. The uncertainty of the texture correlation grid position measurements was ±0.07 μm (±0.05 pixels), based on comparisons of multiple images of stationary microtissues. Subtraction of the initial grid positions obtained from images of the unstretched microtissues yielded the microtissues' deformation field. To correct for position noise caused by mechanical vibrations, three reference $BaTiO_3$ beads were placed outside each well (Figure 3) and their geometrical center was subtracted from both the measured pillar positions and the microtissue displacement field.

2.7. Finite Element Modeling. The boundary of each microtissue was traced from the first frame of the stretching video using a custom script generated in Igor Pro (Wavemetrics). That boundary was then used to define the shape of the microtissue for a 2D linear elastic isotropic finite element model (FEM) generated in COMSOL Multiphysics (COMSOL Inc.), using a plane-stress approximation. The round pillars were modeled as rigid circles that could move in both directions in the horizontal plane, subject to radially directed linear restoring forces $\mathbf{F}_i = -k\mathbf{r}_i$, where $\mathbf{r}_i$ is the vector displacement of the ith pillar. The spring constants were set to be the same as the original PDMS pillar bending constants, and no-slip boundary conditions were imposed at the microtissue−pillar interfaces. Triangular meshes were used for the finite element simulations (Figure S2). (See the Supporting Information for additional details of the models, including discussion of analysis of mesh convergence.) Initial (unstretched) heights of 44 μm (octagonal microtissues) or 60 μm (triangular microtissues) were assumed, based on measurements of typical microtissue heights made with confocal microscopy. For a given magnetic pillar displacement the parameters of the model describing the tissues' Young's moduli were optimized by χ^2 minimization with both the nonmagnetic pillar displacements and the microtissue displacement field data included in the χ^2 cost function, weighted by the relative accuracy of their measurements as given in section 2.6. The minimization was carried out in Matlab using the *Patternsearch* algorithm and calling iterations of the COMSOL FEM from Matlab for each computation of the cost function. Uncertainties in the model parameters for individual fits were estimated from the range for each parameter where χ^2 increased from its minimum value by the factor $(1 + 1/N_{free})$, where $N_{free} = N_{data\text{-}points} - N_{model\text{-}parameters}$ is the number of free parameters.[40] This gave uncertainties of approximately 3% for the moduli of the individual triangular microtissues, and 3% and 10% for the central and edge regions of the individual octagonal microtissues, respectively, as defined in Figure 7. For each microtissue, three fits at equal strain intervals corresponding to 60, 80, and 100 s in the stretching protocol were obtained. The modulus reported for each microtissue was averaged over all such fits.

3. RESULTS

3.1. Effects of Microtissue Geometry on ECM Alignment. Given that fibroblasts remodel their extracellular matrix to align with the principal maximum strains for any given geometry,[20,23] we hypothesized that matrix alignment in microtissues can be controlled by changing the position of the micropillars to constrain the microtissues. To test this possibility, we fabricated μTUG wells with varying sizes and pillar positions and produced HDF microtissues of varying geometries (Figures 1 and 2). As the microtissues formed via cell-mediated compaction of the ECM, the microtissues adopted the shape dictated by the position of pillars in the μTUG wells within 12−24 h, with the cells uniformly

DOI: 10.1021/acsbiomaterials.8b01183
ACS Biomater. Sci. Eng. XXXX, XXX, XXX−XXX

distributed throughout the bodies of the microtissues (Figure S3A, B). Measurements of structural and mechanical properties were made after 72 h to allow the microtissues to stabilize.[28] The microtissue geometries varied from anisotropic shapes, including a triangle (Figure 1A) and elongated rectangles of aspect ratio 4:1 (Figure 1B) and 2:1 (Figure 1C), to more symmetric shapes, including squares (Figure 2A), hexagons (Figure 2B), and octagons (Figure 2C). The microtissues with anisotropic shapes showed high degrees of ECM alignment in their central regions, as is visible from the fibronectin fluorescence images in (Figure 1D−F) and from the corresponding alignment maps (Figure 1G−I).

The resulting angular alignment distribution histograms for single microtissues (Figure 1J, L, N) and averaged over multiple microtissues (Figure 1K, M, O) provide quantitative measures of the spatially averaged ECM alignment. To parametrize the degree of ECM fiber orientation, we fit the averaged angular alignment histograms to a version of the von Mises circular normal distribution function[41,42] with period π to capture the nematic nature of the fiber order

$$P(\theta) = \frac{1}{2\pi}\left(a + b\frac{e^{\kappa\cos 2(\theta-\theta_0)}}{I_0(\kappa)}\right) \quad (1)$$

In this expression, $a + b = 1$ to ensure normalization over the interval $-\pi \le \theta \le \pi$ and $I_0(\kappa)$ is the modified Bessel function of order 0. The effective full width of the peak in $P(\theta)$ is $2\sigma = 1/\sqrt{\kappa}$, and the widths of these distributions varied from 45° to 75°, with the more anisotropic structures yielding greater alignment. The parameters from these fits are listed in Supporting Information Table S2. To give a further sense of this distribution, we define the aligned fraction $f_{||}$ to be the fraction of the fibers' alignment angles that fell within ±30° of the principal orientation direction, and the perpendicular fraction $f_{\perp}$ to be the fraction of alignment angles that fell within ±30° of the perpendicular to the principal direction. For the triangular tissues (Figure 1K), we find $f_{||} = 0.57$ and $f_{\perp} = 0.17$, while, for the 2:1 rectangular geometry (Figure 1O), these numbers were reduced to $f_{||} = 0.42$ and $f_{\perp} = 0.26$, respectively. The corresponding values for all tissue geometries measured are given in Table S2.

The three symmetric shapes (Figure 2) showed substantial regions of unaligned matrix in their centers (Figure 2D−F), with no preferred ordering direction (Figure 2G−I), although they do show bands of local tangential alignment around their edges. The lack of ECM alignment is reflected in the corresponding histograms taken from the central regions (Figure 2J−O). The size of the region with unaligned ECM increased as the number of pillars in the μTUG well increased.

We note that fibronectin immunostaining was used for alignment quantification because: (i) the fibronectin fibers trace the collagen fibers and connect the cells to the collagen network, (ii) the fibronectin immunostaining provided sharper and cleaner images than those from collagen. To confirm that the fibronectin alignment reflected that of the collagen, we measured correlations between immunostained images of both types (Figure S4A, B). The correlation coefficients between these two image types, measured over 21 different microtissues, were calculated both across the whole microtissue body and at their central regions. The correlation coefficients were 0.9 for the whole microtissues and 0.91 for their central regions (Figure S4C), which showed a strong correlation between the fibronectin and the collagen network in these microtissues. In addition, the actomyosin cytoskeletons of individual cells followed the local ECM orientation of the aligned microtissues, as has been seen previously in two-pillar geometries,[28] while those in the unaligned microtissues showed no preferred orientation (Figure S3C,D) To confirm that these ECM alignment effects were not specific to the HDF cells, we also formed microtissues with NIH 3T3 fibroblasts on identically shaped μTUG devices and observed similar microtissue structures and geometry-dependent ECM alignment (Figures S5, S6).

Based on these results, we chose the triangular and the octagonal geometries for further study as representing cases of tissues with unaxially aligned and unaligned ECM, respectively. We also used these microtissues to assess whether the apparent alignment in the microtissues was dependent on the length scale of the observations. Higher resolution confocal imaging of the central regions of both microtissue types (Figure 4A, B) showed greater detail of the ECM fiber organization and alignment (Figure 4D, E) but gave results for quantitative measures of alignment (Figures 4G−H) similar to the lower resolution epifluorescence data in Figures 1 and 2, with a width $2\sigma = 35° \pm 1°$ and aligned fraction $f_{||} = 0.72$ and perpendicular fraction $f_{\perp} = 0.10$ for the triangular tissues (Figure 4G). We also used confocal imaging to probe the regions near the edges of the octagonal microtissues (Figure 4C). Analysis of these regions confirmed the circumferential alignment in those areas (Figures 4F, I), with $2\sigma = 36° \pm 3°$, $f_{||} = 0.56$, and $f_{\perp} = 0.2$. (See Supplementary Table S2 for details of this analysis.) In summary, these structural observations demonstrate that this approach can be used to control matrix alignment in microtissues.

3.2. Microtissue Loading and Mechanical Measurements. In tissues and organs, the architecture and alignment of the ECM determines its mechanical properties.[43] To gain insight into how matrix alignment affects the mechanical properties of microtissues, we generalized the magnetic stretching method previously utilized to infer stiffnesses of two-pillar microtissues[26,28,30] to study our three- and eight-pillar microtissues. Starting from the microtissues' as-grown states, we applied controlled strains via magnetic forces applied to a magnetic sphere adhered to one pillar of each μTUG well. The resulting deflections of the nonmagnetic pillars were used to measure the changes in the microtissues' contractile forces, and a map of the corresponding displacement field within the microtissues was measured via a texture correlation algorithm.[39] The tensile loads were applied over a 110 s interval at a fixed strain rate (0.005−0.05% per second). The triangular microtissues were stretched along their long (alignment) axis. Significant longitudinal deformation was observed near the magnetic pillar where the microtissue was being pulled, and the deformation magnitude decreased with distance from the magnetic pillar (Supporting movies S1 and S2). Figure 5A shows the deformation field and pillar deflections directions of a triangular microtissue 100 s into the loading process. The horizontal (x) and vertical (y) forces F_x and F_y as recorded by the nonmagnetic pillars are shown in Figure 5B, C. Slight lateral compaction was observed near the passive pillars. In this respect, the multipillar triangular microtissues provided more information than the previously studied two-pillar geometries,[26,28,30] as they enabled readout of bidirectional deformation of an aligned microtissue under a tensile load, while the two-pillar devices measure only unidirectional stresses and strains. The net y-force obtained by summing the y-forces

DOI: 10.1021/acsbiomaterials.8b01183
ACS Biomater. Sci. Eng. XXXX, XXX, XXX−XXX

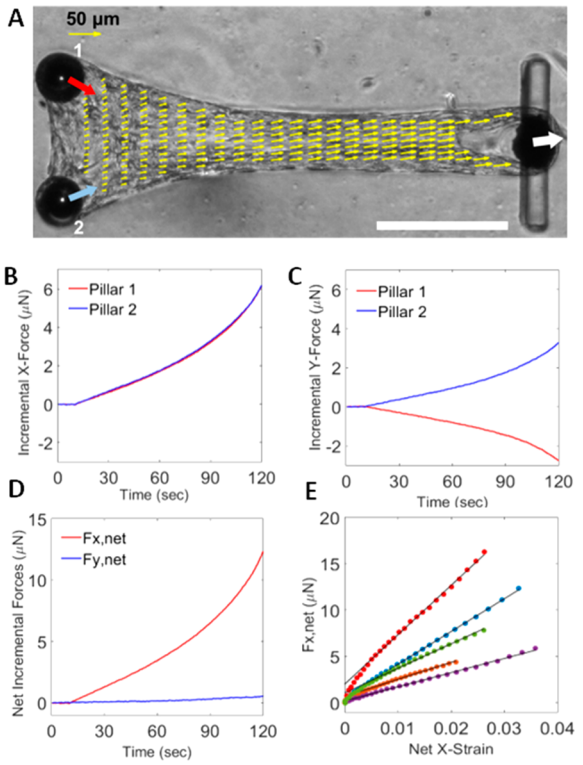

Figure 5. Mechanical response of a triangular microtissue under longitudinal tensile loading (white arrow). (A) The yellow arrows show the deformation field map at a net x-strain of 2.25% at time t = 100 s in the loading protocol. The displacements were measured by texture correlation on a 20 μm × 14 μm rectangular grid but only half the measured points are shown (40 μm × 14 μm spacing). The colored arrows show the nonmagnetic pillars' deflections, magnified by 1100%, and the white arrow shows the magnetic pillar's displacement, magnified by 180% (scale bar = 300 μm). (B, C) Incremental horizontal force $F_x(t)$ and vertical force $F_y(t)$ applied to pillars 1 and 2 by the tissue. (D) Net incremental forces $F_{x,\mathrm{net}}(t)$ and $F_{y,\mathrm{net}}(t)$ summed over the two pillars. (E) $F_{x,\mathrm{net}}$ vs net x-strain plotted for selected triangular tissues. The force vs extension curves are linear with average slope 693 ± 86 μN (N = 18).

from each pillar was much smaller than the net x-force (Figure 5D), but was not exactly zero, as it was not always possible to position the magnetic tweezer to give a purely horizontal force on the magnetic pillar (Figure 5A). Such effects were included in modeling the microtissues to obtain their material properties described in the next section. A useful initial characterization of the microtissues' response to stretching is the net x-force vs the effective net x-strain, which is defined for the triangular tissues in terms of the change in the distance between the magnetic pillar and the average of the x-coordinates of the two nonmagnetic pillars. For the triangular microtissues the net x-force vs effective strain was largely linear over the 0−4% strain range we explored (Figure 5E). The average stiffness estimated from the slopes of the net force vs effective strain curves, and the original measured cross sections of the central region of the microtissues was $\bar{E}$ = 126 ± 16 kPa (N = 18). We note that while this measurement provides evidence that the mechanical response of the microtissues is linear, measures of strain based solely on the pillar positions can be confounded by the behavior of thinner regions present in some microtissues where they loop around the pillars, which can stretch more than the central region of the microtissues. (An example of such a region is visible around the magnetic pillar in Figure 5A.) Thus, the quantitative measurements of material properties described in section 3.3 used the displacement field as measured by the texture correlation approach.

In contrast to the largely longitudinal response of the triangular microtissues, the octagonal microtissues showed both significant longitudinal elongation and lateral compaction. This was apparent in both the local microtissue displacements (Figure 6A and Supporting movies S3 and S4) and in the forces applied by the microtissues to the pillars (Figure 6B, C). The pillars nearest the magnetic pillar (1 and 7 in Figure 6) experienced the largest forces, and the forces on the pillars decreased with distance from the magnetic pillar. The lateral compaction was visible in the y-forces, with pillars above the microtissue midline pulled down while pillars below were pulled up. The nonmagnetic pillar (4) on the midline of the microtissue and also closest to the loading axis did not experience measurable y deflection and force. As the stretching forces were nearly parallel to the microtissues' horizontal axis of symmetry, the net y-force summed over all the pillars was again significantly smaller than the net x-force (Figure 6D). The octagonal microtissues' net x-force vs effective x-strain is shown in Figure 6E, where the "length" for the purpose of the effective strain calculation is taken as the horizontal distance between the magnetic pillar and the nonmagnetic pillar opposite to it along the microtissue's midline (pillar 4 in Figure 6). This effective stress−strain relationship was also observed to be linear for the octagons over the range of deformations applied.

3.3. Material Properties Determination. The micropillar force measurements suggested that both the triangular and octagonal microtissues exhibited a linear force vs extension relationship (Figures 5E and 6E) in the regime of strain (<4%) and strain rates (0.005−0.05% per second) were probed. Hence, we used linear elastic finite element models to parametrize the microtissues' material properties via chi-squared optimization. The Poisson's ratios ν of the microtissues were determined by fixing the moduli and minimizing the chi-squared function. For any value of the moduli, ν asymptotically approached 0.5, the upper limit for linear elastic isotropic materials, indicating incompressibility. Hence for our simulations, we used ν = 0.495. As the mechanical behavior of the triangular microtissues was dominated by the uniaxial extension of the elongated central regions, we approximated these microtissues as a one-material system with one elastic modulus (Figure 7A). The average modulus for these microtissues was found to be E = 139 ± 14 kPa (±SE, N = 25). This is in reasonable agreement with the value $\bar{E}$ estimated from the average slope of the net force vs net strain curves shown in Figure 5E and the measured cross sections of the microtissues' central regions.[28] The displacement field data for a triangular microtissue at 2.25% strain is shown in Figure 7B, and Figure 7C shows the corresponding displacement field obtained from the model. The model overall agreed well with the data as can be seen from the percentage deviations between model and data displacements in Figure 7D. The percentage deviation is somewhat higher near the left edge than in the center of the microtissue, which could be attributed to the left edge having matrix alignment perpendicular to the loading direction. However, the displacement in these regions are an order of magnitude smaller than those of the extreme right and central region of the microtissue and therefore did not contribute significantly to the optimization, which is more sensitive to the

DOI: 10.1021/acsbiomaterials.8b01183
ACS Biomater. Sci. Eng. XXXX, XXX, XXX−XXX

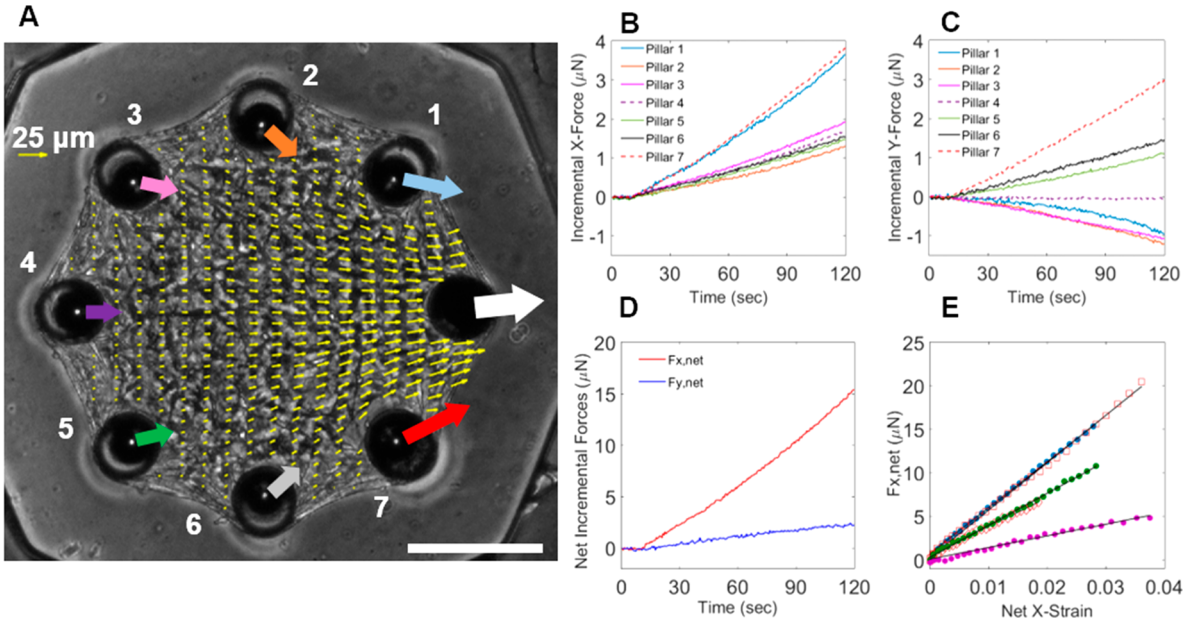

Figure 6. Mechanical response of an octagonal tissue under radial tensile loading (white arrow). (A) Yellow arrows show the deformation field map at an effective net x-strain of 2.25% at time t = 100 s in the loading protocol. The displacements were measured by texture correlation on a 20 μm × 20 μm rectangular grid but only half of the measured points are shown (40 μm × 20 μm spacing). The colored arrows show the nonmagnetic pillars' deflections, magnified by 1500%, and the white arrow shows the magnetic pillar's displacement, magnified by 300% (scale bar = 300 μm). (B, C) Incremental horizontal forces $F_x(t)$ and vertical forcs $F_y(t)$ applied by the tissue to the nonmagnetic pillars identified by the white numbers in panel A. (D) Net incremental forces $F_{x,\mathrm{net}}(t)$ and $F_{y,\mathrm{net}}(t)$ summed over the nonmagnetic pillars. (E) $F_{x,\mathrm{net}}$ vs effective net x-strain plotted for selected octagonal tissues. The effective length is measured as the distance between the magnetic pillar and pillar 4. The force vs extension curves are linear with average slope 451 ± 52 μN (N = 22).

higher deformation regions. Hence the left edge deviations did not affect the determination of the moduli significantly.

Based on the structure of the ECM observed in the octagonal geometry, we parametrized those microtissues as two-material systems, with a central region that encompassed the unaligned portion, and an outer band (Figure 7E) whose boundary was chosen based on the average range of the highly tangentially aligned regions in between the pillars at the microtissues' edges (e.g., Figures 2F and 4C). Preliminary modeling studies showed that reducing the radius of this boundary reduced the quality of the subsequent fits, and so, the boundary was held fixed at its average value and was not varied for individual microtissues. The displacement field for an octagonal microtissue at 2.25% strain, the microtissue's deformation field obtained from the data, and the optimized model along with the percentage deviation of the microtissue and pillar displacements between model and data are shown in Figures 7F–H. The octagons were found to have average modulus for the central region of E_1 = 24 ± 2 kPa, and average modulus for the outer band of E_2 = 145 ± 28 kPa (both ± SE, N = 28). Notably, the central unaligned region was ∼6 times softer than the aligned band, and the modulus of the band was comparable to that seen in the triangular microtissues.

We note that the two-modulus model gave significant improvements over models of the octagonal microtissues with a single modulus (Figure S7). As the two-modulus model showed larger deviations in the outer band than in the central region, we hypothesized that this could be due to the fact that different segments of the band were stretched in different directions relative to their local principal axes of ECM alignment. To test this, we attempted to model the band as an orthotropic material, with different moduli $E_{\parallel}$ and $E_{\perp}$ for deformations parallel and perpendicular to the alignment axis, respectively (Figure S8). However, we found that $E_{\parallel}$ was indistinguishable from the one obtained from the isotropic model, while the fits were insensitive to $E_{\perp}$, showing that, despite the high degree of local matrix alignment near the microtissues' edges, their mechanical behavior was not influenced by $E_{\perp}$.

3.4. Contribution of Cellular Contractility to Matrix Stiffness. To assess the influence of cellular contractility on tissue stiffness in these multipillar geometries, we measured the microtissues' passive contractile forces and their respective elastic moduli before and after a 40 min exposure to the myosin inhibitor blebbistatin at 20 μM concentration. Blebbistatin treatment produced a 70% decrease in the contractile forces generated by both the triangular and octagonal microtissues (Figure 8A). However, no changes in microtissue moduli were observed for either tissue geometry in both the aligned and unaligned regions (Figure 8B). Previous similar studies of two-pillar aligned microtissues reported that contractility inhibition did not affect the tissues' moduli[28,30] and concluded that the stiffness of the microtissues was dominated by the collagen matrix and the passive mechanics of the cellular actin cytoskeletal network, rather than the cells' active contractile machinery. In this study we have thus extended this finding to both aligned and unaligned microtissues. We note that this is distinct from the dynamic response of microtissue constructs[26] and fibroblast-populated collagen gels more broadly,[44−46] where cellular contractility plays an important role in a variety of mechanical properties, including stress shielding and recovery following mechanical perturbations.

We note that the data in Figure 8A also provide a measure of the prestress in the as-grown tissues. For the triangular tissues, the average longitudinal (x) force per tissue in the normal (untreated) state was $\mathbf{F}_L$ = 17 ± 3 μN (±SE, N = 7). From the

DOI: 10.1021/acsbiomaterials.8b01183
ACS Biomater. Sci. Eng. XXXX, XXX, XXX−XXX

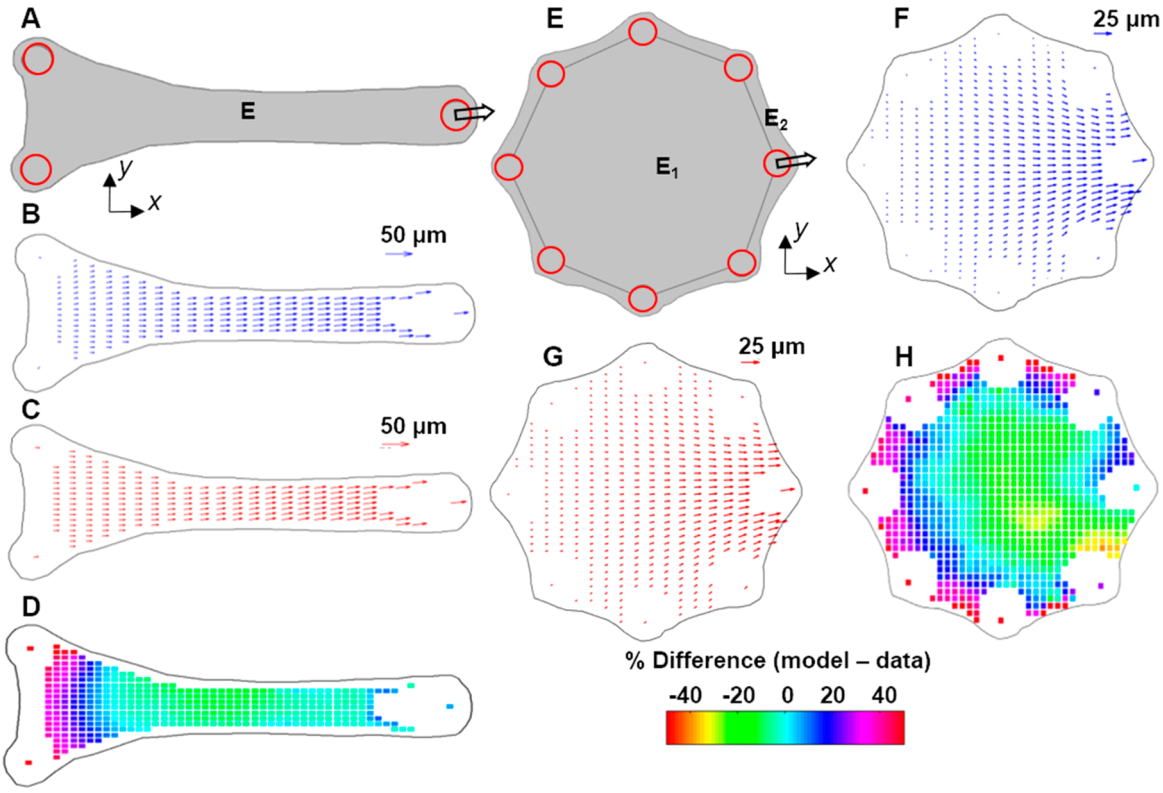

Figure 7. Characterization of microtissues' material properties, utilizing linear elastic finite element modeling. Triangular tissue: (A) FEM shape determined from the phase-contrast image in Figure 3C. The entire tissue body is modeled as a linear elastic isotropic material with an elastic modulus E, with no-slip boundary conditions at the pillars (shown as red circles). (B) Tissue and nonmagnetic pillar displacement data for the magnetic pillar displacement corresponding to a net x-strain of 2.25%. (C) Displacement field obtained from the model. (D) Percentage deviation between the model and data, computed as (model−data)/data. Octagonal tissue: (E) FEM shape determined from a phase image of the tissue (Figure 3D). The octagonal tissue is modeled as a two-material system, with inner region of modulus E_1 an outer band of modulus E_2, and no -slip boundary conditions at the pillars (red circles). (F) Displacement field for the data (net x-strain 2.25%). (G) Corresponding displacement field for the model. (H) Percentage deviation between data and model.

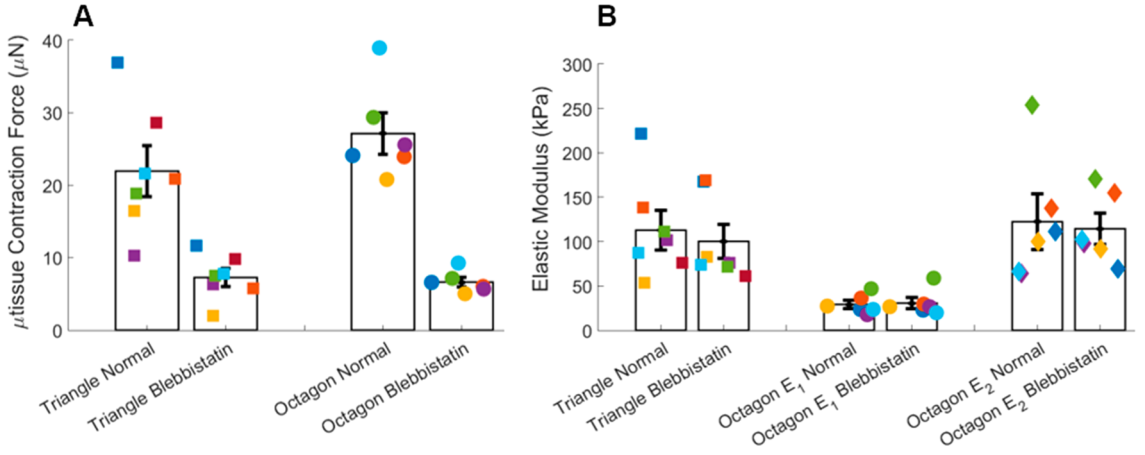

Figure 8. Effects of myosin inhibition via blebbistatin (20 μM) on (A) average contractile force per pillar and (B) microtissue elastic modulus for triangular ($N = 7$) and octagonal ($N = 6$) microtissues. The normal and blebbistatin treated tissue pairs are represented by identical colored symbols in the consecutive bars. (A) $p < 0.001$ for both triangle and octagons via paired t test. (B) $p = 0.34$ for triangles, $p = 0.64$ (E_1), and $p = 0.70$ (E_2). Results are presented as mean ± SE.

average width $w = 100$ μm and thickness $t = 60$ μm of the elongated central regions of those tissues, we estimate a cross-sectional prestress $\sigma_0 = \mathbf{F}_L/(wt) = 2.8 \pm 0.5$ kPa. For the octagonal microtissues, where the average radial force per pillar was $\mathbf{F}_R = 27 \pm 3$ μN (±SE, $N = 6$), we estimate the prestress from the total radial force on all eight pillars $\mathbf{F}_T = 8\mathbf{F}_R$ and the circumferential cross-sectional area at the radius R of the pillars $A = 2\pi Rt$, where $R = 357$ μm and $t = 44$ μm. This yields $\sigma_0 \sim \mathbf{F}_T/A = 1.7 \pm 0.2$ kPa. Relevant to the analysis in the next section, we note that both of these prestress values are much smaller than the respective moduli of those tissues, with $\sigma_0 \sim 0.02E$ for the triangular tissues and $\sigma_0 \sim 0.07E_1$ for the

DOI: 10.1021/acsbiomaterials.8b01183
ACS Biomater. Sci. Eng. XXXX, XXX, XXX−XXX

octagonal tissues. We note that these values and their sizes relative to the tissues' moduli are consistent with previous measurements on fibroblast-populated two-pillar microtissues.[28]

3.5. Comparison to the Distributed Fiber Model. To estimate the effects of the anisotropy in ECM fiber orientation on the differences in the stiffnesses measured in the triangular and octagonal microtissues, we used a distributed fiber anisotropic model developed previously to study native and engineered collagen tissues.[31,32] The approach underlying this model has been widely used to model collagenous tissues.[41,42,47−49] The material is modeled as fibers with a distribution of orientations embedded in an isotropic matrix with shear modulus μ. The fibers are assumed to be identical, characterized by a fiber modulus E_f, and to deform with the continuum. As our model is effectively two-dimensional, the fibers are taken to be confined to the plane of the tissue, with their orientations given by an angular distribution function $D(\mathbf{X}, \theta) = D_0(\mathbf{X})\, P(\theta)$, where $P(\theta)$ is given by eq 1, and $D_0(\mathbf{X})$ is a possibly position-dependent density. (See the Supporting Information for full details of this model.) As our experiments were in a low-strain regime and the prestresses were small compared to the measured moduli (see previous section, 3.4), we linearized the model about zero strain and assumed negligible prestress. In this case the resulting integrals over the fiber distribution $D(\mathbf{X}, \theta)$ can be evaluated analytically, yielding for the modulus along the direction of principal fiber alignment

$$E_{\parallel} = 4\mu + E_f D_0(\mathbf{X}) f_1(a, b, \kappa) - \frac{(2\mu + E_f D_0(\mathbf{X}) f_2(a, b, \kappa))^2}{4\mu + E_f D_0(\mathbf{X}) f_3(a, b, \kappa)} \quad (2)$$

where

$$f_1(a, b, \kappa) = \frac{3}{8}a + b\left(\frac{1}{2} + \frac{(2\kappa - 1)I_1(\kappa)}{4\kappa I_0(\kappa)}\right) \quad (3)$$

$$f_2(a, b, \kappa) = \frac{1}{8}a + b\frac{I_1(\kappa)}{4\kappa I_0(\kappa)} \quad (4)$$

and

$$f_1(a, b, \kappa) = \frac{3}{8}a + b\left(\frac{1}{2} - \frac{(2\kappa + 1)I_1(\kappa)}{4\kappa I_0(\kappa)}\right) \quad (5)$$

where a, b, and κ are the parameters describing the alignment distribution, as in eq 1, and $I_0(\kappa)$ and $I_1(\kappa)$ are modified Bessel functions.

In the case where the fiber orientation distribution is isotropic (i.e., $a = 1$, $b = 0$)

$$E_{\parallel} = E_{iso} = \frac{96\mu^2 + 20\mu E_f D_0(\mathbf{X}) + (E_f D_0(\mathbf{X}))^2}{32\mu + 3E_f D_0(\mathbf{X})} \quad (6)$$

As collagen fibers have been found in other tissue studies[31,42] to dominate the mechanical properties, i.e., $E_f \gg \mu$, we examine this same limit here. In this case, eq 6 reduces to $E_{iso} = E_f D_0(\mathbf{X})/3$, and we can evaluate the more general result for $E_{\parallel}$, eq 2, based on the results of the fits to the fiber orientation distributions $P(\theta)$ (Figures 1−3 and Table S2). Using the data from the confocal images (Figure 4) gives $E_{\parallel,oct} = 0.51 E_f D_0(\mathbf{X})$ for the edge of the octagonal tissue and $E_{\parallel,tri} = 0.64 E_f D_0(\mathbf{X})$ for the long central section of the triangular tissue (Figure S9). While these are enhanced over the isotropic case by up to a factor of ∼2, this is substantially less than the experimentally observed factor of ∼6 enhancement of the aligned regions or these two tissue geometries compared to the isotropic regions in the centers of the octagonal tissues. Indeed, even in the limit where the fibers are fully aligned (i.e., where $P(\theta)$ becomes a Dirac delta function) the model only gives $E_{\parallel,max} = E_f D_0(\mathbf{X})$, a factor of 3 enhancement over the isotropic case. Thus, it appears that while fiber alignment is a significant contributor to the variations in modulus, other factors must also contribute. One such contributing factor is variations in fiber density with position, which should be manifest in spatial variations in integrated intensity in our fluorescence imaging. While it can be difficult to measure density of a stained target accurately from fluorescence intensity alone due to confounding factors such as inhomogeneities in staining efficiency, our epifluorescence imaging shows larger intensity at the tissues' edges than in their centers for both collagen (Figure S4) and fibronectin (Figures 2 and S6). For the octagonal tissues, integrated intensity per unit area in the fibronectin imaging was larger in the edge regions than in the central regions by a factor of 2.6 ± 0.1 (±SE, $N = 6$). Similarly, the integrated intensity per unit area in confocal images (acquired in equal thickness optical sections) in the edge regions of the octagonal tissues is ∼2.5 times larger than that in the central regions (e.g., by comparing the ROIs in Figure 4B, C). These results suggest that changes in local ECM density in these tissues are also a significant contributor to the stiffness differences that we observe.

4. DISCUSSION

Tissue stiffness regulates many cellular processes,[50,51] including stem cell differentiation,[52,53] cell migration,[54,55] cancer metastasis,[56−58] and the progression of fibrosis.[59−62] The concept that substrate stiffness regulates cellular function has emerged due to the advent of synthetic hydrogels with tunable substrate mechanics.[63] While these materials have been instrumental in unraveling how cells sense substrate rigidity, the stiffness of these synthetic materials cannot be modulated by cells in a manner similar to what occurs in native tissues. In contrast, cells embedded in natural ECMs can remodel the ECM and increase stiffness by aligning and cross-linking ECM fibers and increasing the ECM density.

To take advantage of cell-generated ECM modulation, we adapted our previously published μTUG microtissues[24,28] to control and quantify the ECM alignment of self-assembled fibroblast populated microtissues by varying the spacing between the pillar positions. While we have previously shown that this remodeling occurs as a result of myosin-based cellular traction forces,[28,30] the degree of matrix alignment could be controlled by the degree of anisotropy of the boundary constraints as determined by the pillar placements in the μTUG wells. These findings are consistent with other studies that have examined the compaction of cell-laden collagen cells, where the lack of any constraints leads to spherically compacted gel with largely unaligned matrix,[64,65] physically constraining compaction around a mandrel leads to a circumferentially aligned annulus,[66−69] and use of anchor points or pillars leads to differentially aligned structures.[70−72] However, the mechanical consequences of changes in alignment in such structures have not been well characterized.

To measure stiffness in the microtissue system, we induced uniaxial loading of the microtissues via magnetic tweezers. The

DOI: 10.1021/acsbiomaterials.8b01183
ACS Biomater. Sci. Eng. XXXX, XXX, XXX−XXX

resulting force and deformation response of the microtissues, owing to the complex geometry and potentially complex material properties, required a computational modeling approach in order to interpret the findings. Using a simple linear-elastic finite element model provided surprisingly effective descriptions of the microtissue response and allowed a prediction of the effective Young's moduli. Using more complex models did not substantially improve the descriptions, except that it was necessary to consider the edges of the symmetric microtissues (which were highly aligned even in the octagonal microtissues) as distinct from the interior. In this case, we also considered the aligned bands at the microtissues' edges as an orthotropic material (Figure S8) with two moduli: $E_{\parallel}$ and $E_{\perp}$ along and perpendicular to the fiber alignment direction. Even in that setting, despite the ECM alignment, the microtissues' mechanics was insensitive to $E_{\perp}$, and the simple linear elastic model largely agreed with this more complex model, with the finding that the aligned ECM regions of microtissues were six times stiffer than the unaligned regions. Comparison of these results to a linearized distributed fiber anisotropic model[31,32] showed that while the variations in ECM alignment contribute significantly to the variations in modulus between aligned and unaligned regions of the tissues, variations in fiber density is also likely important. Such variations can readily arise from the matrix compaction process during tissue formation.[30] In the seeding process, the μTUG wells are initially uniformly filled with the cell/ECM mixture. As the microtissues form under the cells' contractile force, material initially at the edges of the μTUG wells builds up and is compacted both in the elongated central regions of the triangular tissues and at the boundaries of the more symmetric tissues, as can be seen from both our epifluorescence and confocal imaging. While this compaction process did not yield edge regions that were thicker than the body of the tissues, it did yield some rounding (vertical curvature) of the edges that meant that there was effectively some thickness variation within ~30 μm of the edges. This effect was not included in our model, but we expect its influence to be small in the low-strain range of our experiments and unlikely to change qualitatively the main conclusions of this study. We further note that fiber alignment alone has also been found to be insufficient to explain fully the mechanical anisotropy in larger, cm-scale fibroblast-populated collagen gels, where it was suggested that other anisotropy-induced remodeling processes, such as redistributions of ECM fiber lengths, could be involved.[17] Such effects could potentially also play a role in our system.

5. CONCLUSION

In summary, we have developed an approach to control the alignment of extracellular matrix in engineered microtissues assembled across arrays of pillars in which the alignment is driven by cell-based remodeling as a function of the distribution of pillars. Linear elastic models provide a means to parametrize geometry-dependent stiffness variations in these structures, as confirmed by comparison to an anisotropic distributed fiber model, which also provides insight into the relative importance of ECM fiber alignment and fiber density in determining how the microtissues' architecture impacts their mechanics, in a setting where the composition of the matrix, at least at the outset, is held constant. Such insights will be important in realizing the potential of this new microengineered platform for future explorations of the role of tissue architecture and mechanics in regulating cellular functions.

■ ASSOCIATED CONTENT

Supporting Information

The Supporting Information is available free of charge on the ACS Publications website at DOI: 10.1021/acsbiomaterials.8b01183.

Further descriptions of the finite-element plane stress model used to model the mechanical data, the linearized distributed fiber anisotropic model used to assess the results, and all supplementary figures and tables referred to in the text (PDF)

These four movies illustrate the magnetic stretching of the microtissues and the evolution of the displacement fields with stretch. Supporting movie S1 triangular tissue stretching (AVI)

Supporting movie S2 triangular tissue with displacement map (AVI)

Supporting movie S3 octagonal tissue stretching (AVI)

Supporting movie S4 octagonal tissue with displacement map (AVI)

■ AUTHOR INFORMATION

Corresponding Author

*Email address: reich@jhu.edu.

ORCID

Daniel H. Reich: 0000-0001-6313-9884

Notes

The authors declare no competing financial interest.

■ ACKNOWLEDGMENTS

The experimental work and data analysis were supported by NSF Grants CMMI-1463011 at JHU and CMMI-1462710 at BU. Development of the modeling approaches was supported by a CAREER Award (CMMI-1253453) at JHU.

■ REFERENCES

(1) Shadwick, R. E. Elastic energy storage in tendons: mechanical differences related to function and age. *J. Appl. Physiol.* **1990**, *68* (3), 1033−40.

(2) Cui, L.; Maas, H.; Perreault, E. J.; Sandercock, T. G. In situ estimation of tendon material properties: Differences between muscles of the feline hindlimb. *J. Biomechanics* **2009**, *42* (6), 679−685.

(3) Bennett, M. B.; Ker, R. F.; Imery Nicola, J.; Alexander, R. M. Mechanical properties of various mammalian tendons. *J. Zool.* **1986**, *209* (4), 537−548.

(4) Buchanan, C. I.; Marsh, R. L. Effects of long-term exercise on the biomechanical properties of the Achilles tendon of guinea fowl. *J. Appl. Physiol.* **2001**, *90* (1), 164−71.

(5) Hollenstein, M.; Nava, A.; Valtorta, D.; Snedeker, J. G.; Mazza, E. *Mechanical Characterization of the Liver Capsule and Parenchyma*; Springer: Berlin Heidelberg, 2006; pp 150−158.

(6) Herbert, L. A.; Chen, W. C.; Hartmann, A.; Garancis, J. C. Mechanical properties of the dog renal capsule. *J. Appl. Physiol.* **1976**, *40* (2), 164−70.

(7) Assoul, N.; Flaud, P.; Chaouat, M.; Letourneur, D.; Bataille, I. Mechanical properties of rat thoracic and abdominal aortas. *J. Biomechanics* **2008**, *41* (10), 2227−2236.

(8) Kesava Reddy, G. AGE-related cross-linking of collagen is associated with aortic wall matrix stiffness in the pathogenesis of drug-induced diabetes in rats. *Microvasc. Res.* **2004**, *68* (2), 132−142.

(9) McKee, C. T.; Last, J. A.; Russell, P.; Murphy, C. J. Indentation Versus Tensile Measurements of Young's Modulus for Soft Biological Tissues. *Tissue Eng., Part B* **2011**, *17* (3), 155−164.

DOI: 10.1021/acsbiomaterials.8b01183
ACS Biomater. Sci. Eng. XXXX, XXX, XXX−XXX

(10) Li, Y. L.; Xiao, Y.; Liu, C. S. The Horizon of Materiobiology: A Perspective on Material-Guided Cell Behaviors and Tissue Engineering. *Chem. Rev.* **2017**, *117* (5), 4376−4421.
(11) Girton, T. S.; Dubey, N.; Tranquillo, R. T. Magnetic-induced alignment of collagen fibrils in tissue equivalents. *Methods Mol. Med.* **1998**, *18*, 67−74.
(12) Torbet, J.; Ronzière, M. C. Magnetic alignment of collagen during self-assembly. *Biochem. J.* **1984**, *219* (3), 1057−1059.
(13) Hoogenkamp, H. R.; Bakker, G. J.; Wolf, L.; Suurs, P.; Dunnewind, B.; Barbut, S.; Friedl, P.; van Kuppevelt, T. H.; Daamen, W. F. Directing collagen fibers using counter-rotating cone extrusion. *Acta Biomater.* **2015**, *12*, 113−21.
(14) Matthews, J. A.; Wnek, G. E.; Simpson, D. G.; Bowlin, G. L. Electrospinning of Collagen Nanofibers. *Biomacromolecules* **2002**, *3* (2), 232−238.
(15) Sung, K. E.; Su, G.; Pehlke, C.; Trier, S. M.; Eliceiri, K. W.; Keely, P. J.; Friedl, A.; Beebe, D. J. Control of 3-dimensional collagen matrix polymerization for reproducible human mammary fibroblast cell culture in microfluidic devices. *Biomaterials* **2009**, *30* (27), 4833−41.
(16) Lee, P.; Lin, R.; Moon, J.; Lee, L. P. Microfluidic alignment of collagen fibers for in vitro cell culture. *Biomed. Microdevices* **2006**, *8* (1), 35−41.
(17) Thomopoulos, S.; Fomovsky, G. M.; Chandran, P. L.; Holmes, J. W. Collagen Fiber Alignment Does Not Explain Mechanical Anisotropy in Fibroblast Populated Collagen Gels. *J. Biomech. Eng.* **2007**, *129* (5), 642−650.
(18) Sander, E. A.; Stylianopoulos, T.; Tranquillo, R. T.; Barocas, V. H. Image-based multiscale modeling predicts tissue-level and network-level fiber reorganization in stretched cell-compacted collagen gels. *Proc. Natl. Acad. Sci. U. S. A.* **2009**, *106* (42), 17675−17680.
(19) Wagenseil, J. E.; Elson, E. L.; Okamoto, R. J. Cell Orientation Influences the Biaxial Mechanical Properties of Fibroblast Populated Collagen Vessels. *Ann. Biomed. Eng.* **2004**, *32* (5), 720−731.
(20) Sander, E. A.; Barocas, V. H.; Tranquillo, R. T. Initial fiber alignment pattern alters extracellular matrix synthesis in fibroblast-populated fibrin gel cruciforms and correlates with predicted tension. *Ann. Biomed. Eng.* **2011**, *39* (2), 714−29.
(21) Wakatsuki, T.; Kolodney, M. S.; Zahalak, G. I.; Elson, E. L. Cell mechanics studied by a reconstituted model tissue. *Biophys. J.* **2000**, *79* (5), 2353−2368.
(22) Fernandez, P.; Bausch, A. R. The compaction of gels by cells: a case of collective mechanical activity. *Integrative Biol.* **2009**, *1* (3), 252−259.
(23) Eastwood, M.; Mudera, V. C.; McGrouther, D. A.; Brown, R. A. Effect of precise mechanical loading on fibroblast populated collagen lattices: morphological changes. *Cell Motil. Cytoskeleton* **1998**, *40* (1), 13−21.
(24) Legant, W. R.; Pathak, A.; Yang, M. T.; Deshpande, V. S.; McMeeking, R. M.; Chen, C. S. Microfabricated tissue gauges to measure and manipulate forces from 3D microtissues. *Proc. Natl. Acad. Sci. U. S. A.* **2009**, *106* (25), 10097−102.
(25) Legant, W. R.; Chen, C. S.; Vogel, V. Force-induced fibronectin assembly and matrix remodeling in a 3D microtissue model of tissue morphogenesis. *Integrative Biol.* **2012**, *4* (10), 1164−1174.
(26) Liu, A. S.; Wang, H.; Copeland, C. R.; Chen, C. S.; Shenoy, V. B.; Reich, D. H. Matrix viscoplasticity and its shielding by active mechanics in microtissue models: experiments and mathematical modeling. *Sci. Rep.* **2016**, *6*, 33919.
(27) Xu, F.; Zhao, R.; Liu, A. S.; Metz, T.; Shi, Y.; Bose, P.; Reich, D. H. A microfabricated magnetic actuation device for mechanical conditioning of arrays of 3D microtissues. *Lab Chip* **2015**, *15* (11), 2496−503.
(28) Zhao, R.; Boudou, T.; Wang, W. G.; Chen, C. S.; Reich, D. H. Decoupling cell and matrix mechanics in engineered microtissues using magnetically actuated microcantilevers. *Adv. Mater.* **2013**, *25* (12), 1699−705.
(29) Zhao, R.; Boudou, T.; Wang, W. G.; Chen, C. S.; Reich, D. H. Magnetic approaches to study collective three-dimensional cell mechanics in long-term cultures (invited). *J. Appl. Phys.* **2014**, *115* (17), 172616.
(30) Zhao, R.; Chen, C. S.; Reich, D. H. Force-driven evolution of mesoscale structure in engineered 3D microtissues and the modulation of tissue stiffening. *Biomaterials* **2014**, *35* (19), 5056−64.
(31) Tonge, T. K.; Ruberti, J. W.; Nguyen, T. D. Micromechanical Modeling Study of Mechanical Inhibition of Enzymatic Degradation of Collagen Tissues. *Biophys. J.* **2015**, *109* (12), 2689−700.
(32) Tonge, T. K.; Voo, L. M.; Nguyen, T. D. Full-field bulge test for planar anisotropic tissues: Part II - A thin shell method for determining material parameters and comparison of two distributed fiber modeling approaches. *Acta Biomater.* **2013**, *9* (4), 5926−5942.
(33) Foulds, I. G.; Parameswaran, M. A planar self-sacrificial multilayer SU-8-based MEMS process utilizing a UV-blocking layer for the creation of freely moving parts. *J. Micromech. Microeng.* **2006**, *16* (10), 2109−2115.
(34) Bose, P.; Huang, C. Y.; Eyckmans, J.; Chen, C. S.; Reich, D. H. Fabrication and Mechanical Properties Measurements of 3D Microtissues for the Study of Cell-Matrix Interactions. *Methods Mol. Biol.* **2018**, *1722*, 303−328.
(35) Schneider, C. A.; Rasband, W. S.; Eliceiri, K. W. NIH Image to ImageJ: 25 years of image analysis. *Nat. Methods* **2012**, *9*, 671−675.
(36) Boudaoud, A.; Burian, A.; Borowska-Wykret, D.; Uyttewaal, M.; Wrzalik, R.; Kwiatkowska, D.; Hamant, O. FibrilTool, an ImageJ plug-in to quantify fibrillar structures in raw microscopy images. *Nat. Protoc.* **2014**, *9* (2), 457−63.
(37) Lin, Y.-C.; Kramer, C. M.; Chen, C. S.; Reich, D. H. Probing cellular traction forces with magnetic nanowires and microfabricated force sensor arrays. *Nanotechnology* **2012**, *23* (7), 075101.
(38) Crocker, J. C.; Grier, D. G. Methods of Digital Video Microscopy for Colloidal Studies. *J. Colloid Interface Sci.* **1996**, *179* (1), 298−310.
(39) Zhao, R.; Simmons, C. A. An improved texture correlation algorithm to measure substrate-cytoskeletal network strain transfer under large compressive strain. *J. Biomech.* **2012**, *45* (1), 76−82.
(40) Bevington, P. R. *Data Reduction and Error Analysis for the Physical Sciences*; McGraw-Hill: New York, 1969.
(41) Cortes, D. H.; Lake, S. P.; Kadlowec, J. A.; Soslowsky, L. J.; Elliott, D. M. Characterizing the mechanical contribution of fiber angular distribution in connective tissue: comparison of two modeling approaches. *Biomech. Model. Mechanobiol.* **2010**, *9* (5), 651−658.
(42) Nguyen, T. D.; Boyce, B. L. An inverse finite element method for determining the anisotropic properties of the cornea. *Biomech. Model. Mechanobiol.* **2011**, *10* (3), 323−337.
(43) Fung, Y. C. *Biomechanics: Mechanical Properties of Living Tissues*, 2nd ed.; Springer: New York, 1993.
(44) Elson, E. L.; Genin, G. M. Tissue constructs: platforms for basic research and drug discovery. *Interface Focus* **2016**, *6* (1), 20150095.
(45) Marquez, J. P.; Genin, G. M.; Pryse, K. M.; Elson, E. L. Cellular and matrix contributions to tissue construct stiffness increase with cellular concentration. *Ann. Biomed. Eng.* **2006**, *34* (9), 1475−1482.
(46) Nekouzadeh, A.; Pryse, K. M.; Elson, E. L.; Genin, G. M. Stretch-activated force shedding, force recovery, and cytoskeletal remodeling in contractile fibroblasts. *J. Biomech.* **2008**, *41* (14), 2964−2971.
(47) Billiar, K. L.; Sacks, M. S. Biaxial mechanical properties of the native and glutaraldehyde-treated aortic valve cusp: Part II - A structural constitutive model. *J. Biomech. Eng.* **2000**, *122* (4), 327−335.
(48) Sacks, M. S. Incorporation of experimentally-derived fiber orientation into a structural constitutive model for planar-collagenous tissues. *J. Biomech. Eng.* **2003**, *125* (2), 280−287.
(49) Wan, W.; Dixon, J. B.; Gleason, R. L. Constitutive Modeling of Mouse Carotid Arteries Using Experimentally Measured Microstructural Parameters. *Biophys. J.* **2012**, *102* (12), 2916−2925.
(50) Discher, D. E.; Janmey, P.; Wang, Y.-l. Tissue cells feel and respond to the stiffness of their substrate. *Science* **2005**, *310* (5751), 1139−1143.
(51) Xie, S.-A.; Zhang, T.; Wang, J.; Zhao, F.; Zhang, Y.-P.; Yao, W.-J.; Hur, S. S.; Yeh, Y.-T.; Pang, W.; Zheng, L.-S.; Fan, Y.-B.; Kong, W.;

DOI: 10.1021/acsbiomaterials.8b01183
ACS Biomater. Sci. Eng. XXXX, XXX, XXX−XXX

Wang, X.; Chiu, J.-J.; Zhou, J. Matrix stiffness determines the phenotype of vascular smooth muscle cell in vitro and in vivo: Role of DNA methyltransferase 1. *Biomaterials* **2018**, *155*, 203−216.
(52) Lv, H.; Li, L.; Sun, M.; Zhang, Y.; Chen, L.; Rong, Y.; Li, Y. Mechanism of regulation of stem cell differentiation by matrix stiffness. *Stem Cell Res. Ther.* **2015**, *6* (1), 103.
(53) Engler, A. J.; Sen, S.; Sweeney, H. L.; Discher, D. E. Matrix Elasticity Directs Stem Cell Lineage Specification. *Cell* **2006**, *126* (4), 677−689.
(54) Lo, C. M.; Wang, H. B.; Dembo, M.; Wang, Y. L. Cell movement is guided by the rigidity of the substrate. *Biophys. J.* **2000**, *79* (1), 144−152.
(55) Choquet, D.; Felsenfeld, D. P.; Sheetz, M. P. Extracellular Matrix Rigidity Causes Strengthening of Integrin-Cytoskeleton Linkages. *Cell* **1997**, *88* (1), 39−48.
(56) Paszek, M. J.; Zahir, N.; Johnson, K. R.; Lakins, J. N.; Rozenberg, G. I.; Gefen, A.; Reinhart-King, C. A.; Margulies, S. S.; Dembo, M.; Boettiger, D.; Hammer, D. A.; Weaver, V. M. Tensional homeostasis and the malignant phenotype. *Cancer Cell* **2005**, *8* (3), 241−254.
(57) Reid, S. E.; Kay, E. J.; Neilson, L. J.; Henze, A. T.; Serneels, J.; McGhee, E. J.; Dhayade, S.; Nixon, C.; Mackey, J. B. G.; Santi, A.; Swaminathan, K.; Athineos, D.; Papalazarou, V.; Patella, F.; Román-Fernández, Á.; ElMaghloob, Y.; Hernandez-Fernaud, J. R.; Adams, R. H.; Ismail, S.; Bryant, D. M.; Salmeron-Sanchez, M.; Machesky, L. M.; Carlin, L. M.; Blyth, K.; Mazzone, M.; Zanivan, S. Tumor matrix stiffness promotes metastatic cancer cell interaction with the endothelium. *EMBO J.* **2017**, *36* (16), 2373−2389.
(58) Ahmadzadeh, H.; Webster, M. R.; Behera, R.; Jimenez Valencia, A. M.; Wirtz, D.; Weeraratna, A. T.; Shenoy, V. B. Modeling the two-way feedback between contractility and matrix realignment reveals a nonlinear mode of cancer cell invasion. *Proc. Natl. Acad. Sci. U. S. A.* **2017**, *114* (9), E1617−E1626.
(59) Wells, R. G. Tissue Mechanics and Fibrosis. *Biochim. Biophys. Acta, Mol. Basis Dis.* **2013**, *1832* (7), 884−890.
(60) Liu, F.; Mih, J. D.; Shea, B. S.; Kho, A. T.; Sharif, A. S.; Tager, A. M.; Tschumperlin, D. J. Feedback amplification of fibrosis through matrix stiffening and COX-2 suppression. *J. Cell Biol.* **2010**, *190* (4), 693−706.
(61) Booth, A. J.; Hadley, R.; Cornett, A. M.; Dreffs, A. A.; Matthes, S. A.; Tsui, J. L.; Weiss, K.; Horowitz, J. C.; Fiore, V. F.; Barker, T. H.; Moore, B. B.; Martinez, F. J.; Niklason, L. E.; White, E. S. Acellular Normal and Fibrotic Human Lung Matrices as a Culture System for In Vitro Investigation. *Am. J. Respir. Crit. Care Med.* **2012**, *186* (9), 866−876.
(62) Brown, A. C.; Fiore, V. F.; Sulchek, T. A.; Barker, T. H. Physical and chemical microenvironmental cues orthogonally control the degree and duration of fibrosis-associated epithelial-to-mesenchymal transitions. *J. Pathol.* **2013**, *229* (1), 25−35.
(63) Li, L.; Eyckmans, J.; Chen, C. S. Designer biomaterials for mechanobiology. *Nat. Mater.* **2017**, *16*, 1164−1168.
(64) Grinnell, F. Fibroblast−collagen-matrix contraction: growth-factor signalling and mechanical loading. *Trends Cell Biol.* **2000**, *10* (9), 362−365.
(65) Grinnell, F. Fibroblasts, myofibroblasts, and wound contraction. *J. Cell Biol.* **1994**, *124* (4), 401−404.
(66) Barocas, V. H.; Girton, T. S.; Tranquillo, R. T. Engineered Alignment in Media Equivalents: Magnetic Prealignment and Mandrel Compaction. *J. Biomech. Eng.* **1998**, *120* (5), 660−666.
(67) Hansen, A.; Eder, A.; Bönstrup, M.; Flato, M.; Mewe, M.; Schaaf, S.; Aksehirlioglu, B.; Schwörer, A.; Uebeler, J.; Eschenhagen, T. Development of a Drug Screening Platform Based on Engineered Heart Tissue. *Circ. Res.* **2010**, *107* (1), 35−U70.
(68) Mannhardt, I.; Breckwoldt, K.; Letuffe-Breniere, D.; Schaaf, S.; Schulz, H.; Neuber, C.; Benzin, A.; Werner, T.; Eder, A.; Schulze, T.; Klampe, B.; Christ, T.; Hirt, M. N.; Huebner, N.; Moretti, A.; Eschenhagen, T.; Hansen, A. Human Engineered Heart Tissue: Analysis of Contractile Force. *Stem Cell Rep.* **2016**, *7* (1), 29−42.
(69) Schaaf, S.; Shibamiya, A.; Mewe, M.; Eder, A.; Stöhr, A.; Hirt, M. N.; Rau, T.; Zimmermann, W.-H.; Conradi, L.; Eschenhagen, T.; Hansen, A. Human Engineered Heart Tissue as a Versatile Tool in Basic Research and Preclinical Toxicology. *PLoS One* **2011**, *6* (10), No. e26397.
(70) Foolen, J.; Deshpande, V. S.; Kanters, F. M. W.; Baaijens, F. P. T. The influence of matrix integrity on stress-fiber remodeling in 3D. *Biomaterials* **2012**, *33* (30), 7508−7518.
(71) Stopak, D.; Harris, A. K. Connective tissue morphogenesis by fibroblast traction: I. Tissue culture observations. *Dev. Biol.* **1982**, *90* (2), 383−398.
(72) van Spreeuwel, A. C. C.; Bax, N. A. M.; Bastiaens, A. J.; Foolen, J.; Loerakker, S.; Borochin, M.; van der Schaft, D. W. J.; Chen, C. S.; Baaijens, F. P. T.; Bouten, C. V. C. The influence of matrix (an)isotropy on cardiomyocyte contraction in engineered cardiac microtissues. *Integrative Biol.* **2014**, *6* (4), 422−429.

DOI: 10.1021/acsbiomaterials.8b01183
ACS Biomater. Sci. Eng. XXXX, XXX, XXX−XXX